COMPUTATIONAL RED BONE MARROW DOSIMETRY PHANTOM OF A ONE-YEAR-OLD CHILD ENABLING ASSESSMENT OF EXPOSURE DUE TO INCORPORATED BETA EMITTERS

Sharagin PA[1]✉, Shishkina EA[1,2], Tolstykh EI[1]

[1] Urals Research Center for Radiation Medicine of Federal Medical and Biological Agency, Chelyabinsk, Russia

[2] Chelyabinsk State University, Chelyabinsk, Russia

For residents of territories along the Techa River that was contaminated with radioactive substances in the 1950s, bone-seeking beta-emitting ^{89,90}Sr were the main source of internal exposure of active (red) bone marrow (AM). The dose of these radionuclides conditions the severity of leukemia risk for them. Improvement of the methods of internal AM dosimetry is an important task. Computational 3D phantoms of the skeleton sites are a component of the solution for this task. Simulation of radiation transfer in a heterogeneous bone model allows estimating the dose conversion factors from radionuclide activity to AM dose. This manuscript continues the series of papers covering the development of a set of computational phantoms of a reference human being of different age. The objective of the study was to develop a computational phantom of a one-year-old child skeleton for internal AM dosimetry (exposure due to incorporated beta emitters). Using the original SPSD (stochastic parametric skeletal dosimetry) model, we develop voxel 3D models of skeletal sites. Skeleton sites with active hematopoiesis were modeled as a set of phantoms of simple geometries. Distribution of AM throughout the skeleton and parameters of the phantoms were assessed on the basis of the published results of measurement done in real bones of children aged 9 months to 2 years. The generated computational phantom of a one-year-old child consisted of 39 segments. It simulates the structure of the bone tissue, location of AM, and population variability of the skeleton microstructure and size parameters.

Keywords: trabecular bone, cortical bone, bone marrow dosimetry, computational phantoms, Sr

Funding: the work was part of the Federal Target Program "Ensuring Nuclear and Radiation Safety for 2016-2020 and up to 2035", with financial support from the Federal Medical Biological Agency of Russia.

Author contribution: Sharagin PA — data generation, analysis, interpretation, manuscript authoring and editing; Tolstykh EI — study methodology development, manuscript editing; Shishkina EA — conceptualization, manuscript editing.

✉ **Correspondence should be addressed:** Pavel A. Sharagin
Vorovsky, 68 A, Chelyabinsk, 454141, Russia; sharagin@urcrm.ru

Received: 14.06.2023 **Accepted:** 23.08.2023 **Published online:** 26.09.2023

DOI: 10.47183/mes.2023.030

ВЫЧИСЛИТЕЛЬНЫЙ ФАНТОМ ДЛЯ ДОЗИМЕТРИИ КРАСНОГО КОСТНОГО МОЗГА ГОДОВАЛОГО РЕБЕНКА ОТ ИНКОРПОРИРОВАННЫХ БЕТА-ИЗЛУЧАТЕЛЕЙ

П. А. Шарагин[1]✉, Е. А. Шишкина[1,2], Е. И. Толстых[1]

[1] Уральский научно-практический центр радиационной медицины Федерального медико-биологического агентства, Челябинск, Россия

[2] Челябинский государственный университет, Челябинск, Россия

Остеотропные бета-излучающие изотопы стронция (^{89,90}Sr) были основными источниками внутреннего облучения красного костного мозга (ККМ) для жителей прибрежных территорий реки Течи, подвергшейся радиоактивному загрязнению в 1950-е годы. Именно с дозой этих частиц связан повышенный риск лейкозов в когорте жителей ее прибрежных территорий. Важной задачей является совершенствование внутренней дозиметрии облучения ККМ. Она включает в себя разработку вычислительных фантомов, представляющих собой трехмерные модели участков скелета. Имитация переноса излучения в гетерогенной модели кости позволяет оценить коэффициенты перехода от активности радионуклида в кости к дозе на ККМ. Эта статья является продолжением работы по созданию набора вычислительных фантомов скелета людей разного возраста. Целью работы было разработать вычислительный фантом скелета годовалого ребенка для внутренней дозиметрии ККМ от инкорпорированных бета-излучателей. С помощью оригинальной методики SPSD (stochastic parametric skeletal dosimetry) создавали трехмерные модели участков скелета в воксельной форме. Участки скелета с активным гемопоэзом моделировали как набор фантомов простой геометрической формы. Распределение ККМ в скелете, а также параметры фантомов оценивали на основе опубликованных результатов измерений реальных костей детей в возрасте от 9 месяцев до 2 лет. Для годовалого ребенка был сгенерирован вычислительный фантом, состоящий из 39 сегментов. Он имитирует структуру костной ткани и положение ККМ, а также популяционную вариабельность параметров микроструктуры и размеров скелета.

Ключевые слова: трабекулярная кость, кортикальная кость, дозиметрия костного мозга, вычислительные фантомы, Sr

Финансирование: работа выполнена в рамках реализации Федеральной целевой программы «Федеральная целевая программа «Обеспечение ядерной и радиационной безопасности на 2016–2020 годы и на период до 2035 года» и при финансовой поддержке Федерального медико-биологического агентства России.

Вклад авторов: П. А. Шарагин — получение, анализ и интерпретацию данных, написание и редактирование статьи; Е. И. Толстых — разработка методики исследования, редактирование статьи; Е. А. Шишкина — разработка концепции, редактирование статьи.

✉ **Для корреспонденции:** Павел Алексеевич Шарагин
ул. Воровского, д. 68 А, г. Челябинск, 454141, Россия; sharagin@urcrm.ru

Статья получена: 14.06.2023 **Статья принята к печати:** 23.08.2023 **Опубликована онлайн:** 26.09.2023

DOI: 10.47183/mes.2023.030

Radionuclide incorporation in a human body could lead to internal exposure of tissues and organs. One of the most radiosensitive organs is the haematopoietically active bone marrow (AM). Found inside skeletal cavities, AM cells are the main target for bone-seeking radionuclides that accumulate in mineralized bone tissue. The most dangerous of the radionuclides are ^{89,90}Sr. These very radionuclides were the key source of AM exposure for the residents of the Techa riverside settlements, contaminated with radioactive substances in the 1950s. Mean AM dose absorbed in the course of a lifetime in the Techa River Cohort members was 0.35 Gy, but in some people it exceeded 1 Gy and could reach 7 Gy, which resulted in a chronic radiation

syndrome development and raised the risk of leukemia [1–4]. The contribution to the AM dose was 61–94% and 2.5–3.2% of ^{90}Sr and ^{89}Sr, respectively [5]. Among the exposed individuals are people of various ages, including small children. Dose assessment for the exposed population could help to prepare for potential radiation emergencies. The methods of dosimetric modeling that were used previously to estimate AM dose are outdated [6]. More accurate data on AM doses received by the members of the Southern Urals population exposed to radiation cohort (SUPER cohort) would allow better assessment of the radiation-related risks of leukemias [7]. Estimation of the AM doses requires assessment of the radionuclide specific activity in the source tissue and calculation of the dose conversion factor (*DF*) from specific activity of a radionuclide in the source to the absorbed dose rate in a target.

Biokinetic models that describe distribution and transfer of a radionuclide through the tissues of the body after its ingress are used to estimate radionuclide specific activity [5]. *DF* is calculated using dosimetric modeling. It involves simulating the transfer of radiation resulting from strontium isotopes decay in the source tissue (bone) and energy absorption in AM (the target tissue), taking into account the exposure geometry. That is why an important part of dosimetric modeling is the elaboration of computational bone phantoms. They are surrogates of the real body tissues (AM and bone) that describe the geometry of source and target tissues and allow simulation of radiation transfer. It should be noted that the current approaches to modeling shape and structure of the bone are based on the analysis of postmortem computed tomography (CT) images of individual bone segments [6, 8–12]. The use of autopsy material limits the number of samples used to estimate the parameters of phantoms and makes it impossible to account for individual variability of size of human bones.

An original parametric method of stochastic modeling of bone structures, SPSD modeling (SPSD — stochastic parametric skeletal dosimetry), was developed at the Urals Research Center for Radiation Medicine [13]. SPSD modeling implies determination of parameters of the phantoms based on numerous published bone measurements. It allows accounting for the uncertainties due to the variability of skeletons in different people. The inside of a computational bone phantom is filled with spongiosa, which is a combination of trabecular bone and AM. And its outside bears a dense layer of cortical bone. The trabecular bone is modeled as a grid of rod-like trabeculae. Such model is a simplified representation of a real bone, yet it is suitable for internal dosimetry of bone-seeking beta-emitters [13]. The previously published numerical experiments [14, 15] demonstrate adequacy of the model; these experiments yielded energy dependences for SPSD phantoms that were compared to the published data [12].

The current study is devoted to the elaboration of a computational phantom of a one-year-old child's skeleton. It is the next step in the series of studies on the development of a set of computational phantoms of a reference man of different age. Previously, we published a paper covering the development of the computational phantom of a newborn's skeleton [16].

The objective of the study is the elaboration of a computational phantom of skeleton of a one-year-old child to estimate AM doses due to beta-emitting radionuclides incorporated in the bone.

METHODS

The phantoms were created using the original SPSD method. For dosimetric modeling, we selected only the skeletal sites with active hematopoiesis. A set of hematopoietic sites were identified based on the published data on AM distribution inside the skeleton [17]. SPSD phantom of skeletal hematopoietic sites consists of a set of smaller phantoms, which are basic phantoms of bone segment (BPS) of simple geometry. They describe individual sites of the skeletal bones. The approach to determination of BPS parameters (based on the previously published data) is given below.

We studied papers in peer-reviewed journals, atlases, manuals, monographs and dissertations as sources of data on dimensional characteristics of bones of a one-year-old child. This set was completed with electronic resources containing collections of X-ray images. The measurements of people/samples that the authors qualified as healthy without diseases leading to bone deformation were collected for the analysis. The ethnicities considered were Caucasians and Mongoloids, as these groups are common in the Ural region. The age of the children ranged from 9 months to 2 years.

Relying on the published data, for every hematopoietic site we assessed linear dimensions and thickness of the cortical bone layer (*Ct.Th.*), as well as bone microarchitecture characteristics: trabeculae thickness (*Tb.Th.*), trabecular separation (*Tb.Sp*), bone volume fraction of spongiosa (*BV/TV*). The linear skeletal bone measurements obtained using callipers, osteometric boards, ultrasound and X-ray examinations, and CT were studied. Histomorphometry and micro-CT data were used to assess the parameters of trabecular bone (*Tb.Th.*, *Tb.Sp*, *BV/TV*) and cortical layer thickness.

Averaged estimates of bone characteristics were taken as parameters for digital phantoms. If published papers containing data on individual measurements were available, we combined them and calculated arithmetic means and standard deviations (SD). When the data on the study of the groups of people were averaged, then for each group we used a weighting factor, (W_N), that factored in the number (N) of samples: $W_N = 1$ if $N \geq 25$; $W_N = N/25$ if $N < 25$. The methods of selection and analysis of the published data were described in detail in previous publications [18–21].

Having acquired the datasets presenting population-average characteristics of bone size and shape, we divided each hematopoietic site into small segments of simple geometric shape with homogeneous bone microarchitecture and cortical layer thickness. Such segmentation allows accounting for heterogeneity of structure of trabecular and cortical bone inside a single hematopoietic site and simplifies modeling. The process of segmentation has been described in detail in [18, 19].

Each phantom includes descriptions of the modeled media and geometry of source and target tissues. Bone marrow (BM) and mineralized bone tissue (part of trabecular and cortical bone) are the media constituting BPS. Chemical composition and density of the modeled media were determined based on the previously published data [22] and applied for all phantoms of a one-year-old child.

For each segment a voxel BPS was generated in the Trabecula [23] software. Depending on the position of the center of the voxel in the phantom, voxels imitate either mineralized bone or bone marrow (BM). We regarded trabecular bone (TB) and cortical bone (CB) as source tissues, and bone marrow (BM) as a detector tissue. BM was uniformly distributed between trabeculae inside the BPS. Voxel sizes differed phantom to phantom, but did not exceed 70% of the trabecula thickness [23, 24]. In the modeled phantoms, the size of the voxel varied in the range from 50 to 200 μm. Trabecula software automatically calculated the volumes of source and detector tissues for each BPS.

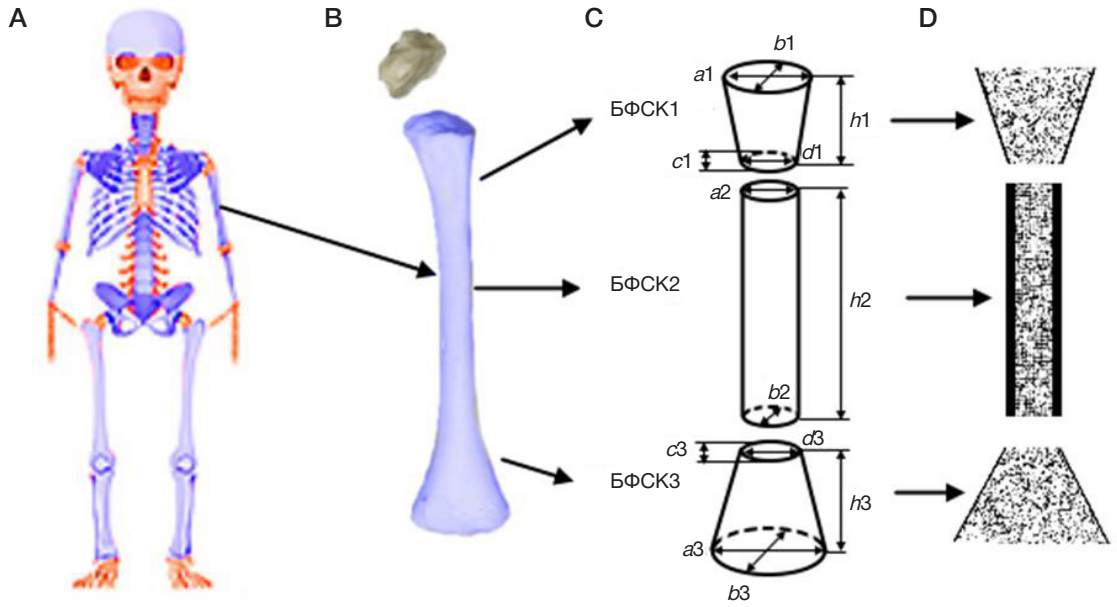

Fig. Segmentation of a hematopoietic site of a one-year-old child's skeleton using the example of humerus. **A**. Skeleton of a one-year-old child (active hematopoietic sites are highlighted blue). **B**. Humerus. **C**. *Pattern* of division of the bone into BPSs and their dimensions. **D**. BPS of humerus in voxel representation, a sectional view (*black* voxels imitate bone, *white* — BM)

Hematopoietic sites of a one-year-old child, division into segments and modeled BPS are demonstrated on the example of the humerus (Figure).

To simulate population variability of dimensions and microstructure characteristics, we generated 12 SPSs (supplementary phantoms) for each BPS with mean parameter values. The parameters of these SPSs were selected at random, within the range of their individual variability (within the limits of minimum and maximum values of the measurements).

RESULTS

The main hematopoietic sites in a one-year-old child's skeleton and the AM mass fraction therein, were determined in accordance with the MRI data [17] (Table 1).

According to Table 1, skeleton of a one-year-old child includes 13 hematopoietic sites for modeling. The AM mass fraction therein ranges from 0.9 to 28.7% of its total mass fraction in the body.

As is the case with a newborn [16], the following parts of the skeleton were not modeled: epiphysis of the tubular bone, sternum, craniofacial bones and vertebral processes (cervical, thoracic, lumbar), because, according the published data [26–31], they either contain very little AM or consist of cartilage tissue.

Table 2 presents chemical composition of the modeled media; we selected the values based on the ICRP data [22] for adults.

The density of mineralized bone tissue was calculated based on the published measurement results of the cortical bone density of one-year-old children [25]; it made up 1.70 g/cm^3. As for the red bone marrow, its density was taken as equal to that of water, 1 g/cm^3 [16].

The parameters of spongiosa were also determined based on the published data; their analysis and calculation of population-average spongiosa parameters were described in detail in [21]. Table 3 presents the values of the BPSs micro-architecture parameters of a one-year-old child.

Table 4 presents linear dimensions and cortical layer thickness assumed for BPSs of a one-year-old child.

The phantom of hematopoietic sites of a newborn's skeleton consists of 39 BPSs (Table 4). Depending on the shape of the simulated hematopoietic sites, we used different amount of BPSs to describe them: from 1 (ribs) to 9 (sacrum).

Table 1. AM mass fraction (% of the total AM mass fraction in the skeleton) in the main hematopoietic sites of a one-year-old child's skeleton [15].

№	Hematopoietic site	AM mass fraction, %
1	Femur	8.1
2	Humeri	5.2
3	Sacrum	5.1
4	Tibia bones	8.7
5	Pelvic bones	13.1
6	Skull	28.7
7	Clavicle	0.9
8	Scapula	2.7
9	Ribs	8.2
10	Radius and ulna	2.6
11	Cervical vertebrae	2.1
12	Thoracic vertebrae	8.3
13	Lumbar vertebrae	6.4

Table 2. Chemical composition of the modeled media (all BPS)

Chemical composition, relative untis		
Chemical element	Bone	Bone marrow
H	0.035	0.105
C	0.16	0.414
N	0.042	0.034
O	0.445	0.439
Na	0.003	0.001
Mg	0.002	0.002
P	0.095	0.002
S	0.003	0.002
Ca	0.215	–

For the most part, BPSs were modeled by cylinders and rectangular parallelepipeds. The size of the phantoms varies widely, from 2.7 to 35.8 mm. Phantoms describing spinal column have no cortical layer due to the fact that the ossification process is incomplete (Table 4). Bodies of femur and tibia have the highest values of *Ct.Th.* for the BPS of a one-year-old child: 2.3 mm. In the first year of life, bones of the cranial vault ossify intensively and the fontanelles close up, therefore, as opposed to those of a newborn, BPSs representing cranial vault of a one-year-old child are covered with a cortical bone layer. The spongiosa parameters differed significantly for different BPSs. The *BV/TV* ratio in BPSs varies from 14 to 52%, *Tb.Th.* value — from 0.09 to 0.29 mm, *Tb.Sp* value — from 0.48 to 0.98 mm (Table 3).

Individual variability of the BPSs dimensional parameters on the average made up 14%, with the highest value belonging to the scapula acromion (42%) and the lowest — to the acetabulum of pubic bone (3%). On the average variability of the cortical layer thickness made up 20%, with the maximum 47% variability for iliac ala. The mean variability of spongiosa parameters was 25%, with minimum and maximum values 9% and 52%, respectively.

The variability values were used to model the SPSs. Their volumes vary widely; they can be 3-fold larger or smaller than those of the BPSs. Further on, we shall calculate DF both for BPSs and SPSs. Mean square deviation of DF calculated for SPSs from those calculated for BPS will characterize the population variability of the DF.

DISCUSSION

In the study devoted to the modeling of a newborn's skeleton [16], we have demonstrated that the weight of the generated phantoms correspond to the weight of real bones. We could not make such a comparison for the phantom of a one-year-old child's skeleton due to lack of data on weight of the respective wet bones in the available literature. However, it is interesting to compare skeletal phantoms of a one-year-old child and a newborn. In general, the former includes more BPSs than the latter, which counts 34 of them. This is due to the ossification and increase in the size of sacrum, which required additional segmentation of the ilium. At the same time, in the bones of hands and feet, yellow bone marrow replaces AM already in the first year of life, which means these segments are not modeled when a one-year-old child's phantom is elaborated.

Naturally, the volume of similar BPSs increases with age, along with the size of the bones. The comparison of the volume of the phantoms of the skeletal sites of a newborn and one-year old child based on the example of distal femur, clavicle, cervical and lumbar vertebral bodies is given in table 5.

The volume of BPSs in the phantom of a one-year-old child is significantly higher than in that of a newborn (Table 5). The volumes of the modeled media also increase in the vast majority of phantoms. Interestingly, if the source tissue volume (TB and CB) increases 1.5 times on the average, the volume of the target tissue increases in 4.5 times. The drop in the volume of trabecular bone (TB) in the lumbar vertebral body phantoms

Table 3. Spongiosa parameters assumed for BPSs of a one-year-old child [32–42] (CV is given in parentheses, %)

Hematopoietic site	*BV/TV*, %	*Tb.Th.*, mm	*Tb.Sp*, mm
Femur	22 (32)	0.16 (38)	0.54 (20)
Humeri	22 (32)	0.17 (17)	0.58 (47)
Ribs	29 (34)	0.23 (35)	0.51 (14)
Tibia	20 (15)	0.09 (9)	0.74 (11)
Pelvis	23 (13)	0.12 (20)	0.48 (23)
Skull	52 (10)	0.29 (31)	0.57 (35)
Clavicle*	29 (31)	0.15 (13)	0.80 (25)
Ulna and radii*	16 (31)	0.13 (15)	0.77 (16)
Scapulae*	22 (36)	0.19 (52)	0.96 (23)
Cervical vertebrae	20 (20)	0.18 (13)	0.60 (20)
Thoracic vertebrae + Lumbar vertebrae + Sacrum	14 (29)	0.10 (42)	0.60 (20)

Note: * — spongiosa parameters calculated based on measurements of similar bones or data for other ages; the method of calculation has been described previously [20].

Table 4. Linear dimensions and cortical layer thickness assumed for BPSs of a one-year-old child

Hematopoietic site	Segment	Shape[1]	Parameters of phantom, mm (CV in parentheses, %)[2]						References
			h	*a*	*b*	*c*	*d*	*Ct.Th.*	
Femur	Diaphysis[4]	c	30	11.2 (7)	11.2 (7)			2.3 (17)	43–47
	Proximal end	dc	35.8 (4)	34 (12)	18 (8)	11.2 (7)	11.2 (7)	0.7 (17)	
	Distal end	dc	35.8 (4)	34 (12)	18 (8)	11.2 (7)	11.2 (7)	0.6 (17)	
Humeri	Diaphysis[4]	c	30	9.1 (13)	9.1 (13)			1.6 (19)	43, 45, 47, 48
	Proximal end	dc	16 (13)	19.8 (13)	19.8 13)	9.1 (13)	9.1 (13)	0.5 (20)	
	Distal end	dc	16 (13)	19.8 (16)	9.1 (13)	9.1 (13)	9.1 (13)	0.4 (20)	
Ribs	Ribs[4]	p	8.7 (32)	30	3.9 (35)			0.5 (33)	49, 50
Sacrum	Body of the 1st vertebra	p	9.2 (20)	25.2 (10)	12.5 (10)				51–55
	Body of the 2nd vertebra	p	9.2 (20)	20.2 (10)	10 (10)				
	Body of the 3rd vertebra	p	8.3 (20)	15.1(10)	8.8 (10)				
	Body of the 4th vertebra	p	5.5 (20)	15.1 (10)	8.8 (10)				
	Body of the 5th vertebra	p	5.5 (20)	12.6 (10)	5 (10)				
	Ala of the 1st vertebra	p	9.2 (20)	10.7 (10)	12.5 (10)				
	Ala of the 2nd vertebra	p	9.2 (20)	8 (10)	10 (10)				
	Ala of the 3rd vertebra	p	8.3 (20)	8 (10)	8.8 (10)				
	Ala of the 4th vertebra	p	5.5 (20)	5.4 (9)	8.8 (10)				
Tibia bones	Fibula[4]	c	30	4.4 (11)	4.4 (11)			1.2 (17)	56
	Tibia diaphysis[4]	c	30	9 (13)	9 (13)			2.3 (9)	55–58
	Tibia proximal end	dc	38.9 (6)	27.2 (12)	15.2 (18)	9 (13)	9 (13)	0.5 (14)	
	Tibia distal end	dc	22.3 (6)	16.8 (23)	16.8 (23)	9 (13)	9 (13)	0.5 (14)	
Pelvic bones	Iliac bone part 1[3]	p	5 (18)	30	30			1.2 (33) 0.5 (47)	59–64
	Iliac bone part[2]	p	5 (18)	30	30			0.4 (30)	
	Acetabular part of iliac bone	dc	14.5 (10)	26.1 (9)	10 (30)	23.6 (22)	17.8 (40)	0.4 (30)	
	Acetabular part of pubic bone	c	4.8 (15)	15.5 (3)	10.9 (7)	7.7 (11)	7.7 (11)	0.4 (30)	
	Pubic ramus superior	c	19.3 (15)	7.7 (11)	7.7 (11)			0.4 (30)	
	Acetabular part of ischium	p	17.5 (15)	17.5 (15)	17.8 (30)	17.5 (15)		0.4 (3)	
	Ischium tuberosity	c	13 (15)	11.7 (15)	11.9 (15)			0.4 (3)	
Skull	Flat bones[4]	p	2.7 (30)	30	30			0.7 (29)	65–68
Clavicle	Body	c	42.2 (11)	7.2 (10)	5.2 (10)			0.9 (10)	69–72
	Sternum end	dc	7.4 (11)	14.1 (10)	12.7 (9)	7.2 (10)	5.2 (10)	0.4 (10)	
	Acromial end	dc	7.4 (11)	12.1 (10)	7.2 (19)	7.2 (10)	5.2(10)	0.4 (10)	
Radius and ulna	Diaphysis[4]	c	30	5.3 (6)	5.3 (6)			1.1 (13)	46, 56, 57
	End	dc	16.2 (6)	8 (6)	5.3 (6)	5.3 (6)	5.3 (6)	0.4 (29)	
Scapula	Glenoid	c	6.8 (26)	17.5 (18)	10.2 (29)			0.5 (29)	73–77
	Acromion	p	7 (19)	16 (41)	13 (42)			0.4 (13)	
	Body[4]	p	2.7 (13)	30	30			0.4 (13)	
Cervical vertebrae	Vertebral body	c	5.8 (9)	9.7 (7)	12.6 (7)				78, 79
Thoracic vertebrae	Vertebral body	c	8 (15)	11.9 (13)	15 (23)				78, 80
Lumbar vertebrae	Vertebral body	c	9.6 (16)	9.6 (16)	21 (3)				78, 53

Note: [1] — the shape of a phantom was designated as follows: *c* — cylinder, dc — deformed cylinder, *p* — rectangular parallelepiped, *e* — ellipsoid; [2] — dimensions of the BPSs: *h* — height; *a* — major axis (c), major axis for a larger base (dc) or side a (r); *b* — minor axis (c), minor axis for a larger base (dc) or side b (r); *c* — major axis for smaller base (dc); *d* — minor axis for smaller base (dc); for ellipsoid (e), *a*, *b*, *c* are the axes; [3] — different cortical layer thickness values were taken for inner (medial) and outer (gluteal) surfaces of this segment of the iliac bone (see Figure); [4] — BPS simulated only part of a modeled bone segment when dimensions thereof significantly exceeded 30 mm, since in such cases from the point of view of dosimetry it makes no sense to model the entire segment [13, 16].

Table 5. Comparison of the volumes of BPSs, newborn and one-year-old child

BPSs	Modeled media	Volume of the modeled structure, cm^3		
		Newborn	One-year-old	One-year-old / newborn
Tibia distal end	*BM*	1.36	6.53	4.80
	TB	0.79	1.88	2.38
	CB	0.37	1.41	3.81
	Entire BPS	2.52	9.82	3.90
Clavicle sternal end	*BM*	0.19	0.35	1.84
	TB	0.08	0.14	1.75
	CB	0.05	0.09	1.80
	Entire BPS	0.32	0.58	1.81
Lumbar vertebra body	*BM*	0.36	1.32	3.67
	TB	0.29	0.2	0.69
	Entire BPS	0.65	1.52	2.34
Cervical vertebra body	*BM*	0.06	0.45	7.50
	TB	0.08	0.11	1.38
	Entire BPS	0.14	0.56	4.00

is explained by the decreasing BV/TV ratio: according to the published data, it goes down from 0.45 to 0.14 (Table 3). In most BPSs, the volume of CB increases significantly, 2.3-fold on the average, in the first year of life, with the exception of BPSs of vertebral bodies. On the average, the total volume of BPSs for a one-year-old child is 2.4 times larger than that for a newborn.

CONCLUSIONS

As a result of this study computational phantoms of the main sites of a one-year-old child's skeleton with active hematopoiesis were created. We developed these phantoms using the same methods as for the phantoms of a newborn. The generated phantoms simulate bone tissue structure and population variability of the size of individual bone structure. The presented phantom of a one-year-old child will be used to calculate DF for $^{89,90}Sr$, which in turn are necessary to estimate refined factors linking individual intake of the radionuclide and the AM dose, which will help to improve dose estimates for residents of the Ural region. It should be noted that the phantom developed with the help of SPSD could be used to calculate DF for other bone-seeking beta emitters, including those used in radionuclide therapy, such as ^{89}Sr, ^{32}P, ^{186}Re, ^{188}Re, ^{117}mSn. Our plans include generation of SPSD skeletal phantoms for other age groups: 5-year, 10-year, 15-year old children and adults. SPSD phantoms can be used for dosimetry of incorporated bone-seeking beta-emitters in the population in situations when the environment is contaminated with radionuclides.

References

1. Degteva MO, Shagina NB, Vorobiova MI, Shishkina EA, Tolstykh EI, Akleyev AV. Contemporary Understanding of Radioactive Contamination of the Techa River in 1949-1956. Radiats Biol Radioecol. 2016; 56 (5): 523–34.PMID: 30703313. Russian.
2. Krestinina LY, Epifanova S, Silkin S, Mikryukova L, Degteva M, Shagina N, et al. Chronic low-dose exposure in the Techa River Cohort: risk of mortality from circulatory diseases. Radiat Environ Biophys. 2013; 52 (1): 47–57. DOI: 10.1007/s00411-012-0438-5. Epub 2012 Nov 4.
3. Akleev AV. Hronicheskij luchevoj sindrom u zhitelej pribrezhnyh sel reki Techa. Chelyabinsk: Kniga, 2012; 464 s. Russian.
4. Preston DL, Sokolnikov ME, Krestinina LY, Stram DO. Estimates of radiation effects on cancer risks in the mayak worker, Techa river and atomic bomb survivor studies. Radiat Prot Dosimetry. 2017; 173 (1–3): 26–31. DOI: 10.1093/rpd/ncw316.
5. Degteva MO, Napier BA, Tolstykh EI, et al. Enhancements in the Techa river dosimetry system: TRDS-2016D Code for reconstruction of deterministic estimates of dose from environmental exposures. Health Phys. 2019; 117 (4): 378–87. DOI: 10.1097/HP.0000000000001067.
6. Spiers FW, Beddoe AH, Whitwell JR. Mean skeletal dose factors for beta-particle emitters in human bone. Part I: volume-seeking radionuclides. The British journal of radiology. 1978; 51 (608): 622–7.
7. Silkin SS, Krestinina LYu, Starcev NV, Akleev AV. Ural'skaya kogorta avarijno-obluchennogo naseleniya. Medicina ehkstremal'nyh situacij. 2019; 21 (3): 393–402. Russian.
8. O'Reilly SE, DeWeese LS, Maynard MR, Rajon DA, Wayson MB, Marshall EL, et al. An 13 image-based skeletal dosimetry model for the ICRP reference adult female-internal electron 14 sources. Phys Med Biol. 2016 Dec 21; 61 (24): 8794–824. Epub 2016 Nov 29.
9. Xu XG, Chao TC, Bozkurt A. VIP-Man: an image-based whole-body adult male model constructed from color photographs of the Visible Human Project for multi-particle Monte Carlo calculations. Health Phys. 2000; 78 (5): 476–86. DOI: 10.1097/00004032-200005000-00003. PMID: 10772019.
10. Shah AP, Bolch WE, Rajon DA, Patton PW, Jokisch DW. A paired-image radiation transport model for skeletal dosimetry. J Nucl Med. 2005; 46 (2): 344–53. PMID: 15695796.
11. Pafundi D. Image-based skeletal tissues and electron dosimetry models for the ICRP reference pediatric age series. A dissertation presented to the graduate schools of the University of Florida in partial fulfillment of the requirements for the degree of doctor of the philosophy. University of Florida. 2009.
12. Hough M, Johnson P, Rajon D, Jokisch D, Lee C, Bolch W. An image-based skeletal dosimetry model for the ICRP reference adult male–internal electron sources. Phys Med Biol. 2011; 56 (8): 2309–46. DOI: 10.1088/0031-9155/56/8/001.
13. Degteva MO, Tolstykh EI, Shishkina EA, Sharagin PA, Zalyapin VI, Volchkova AYu, et al. PLoS One. 2021; 16 (10): e0257605.

DOI: 10.1371/journal.pone.0257605. PMID: 34648511; PMCID: PMC8516275.PlosOne.
14. Dyogteva MO, Shishkina EA, Tolstykh EI, Zalyapin VI, Sharagin PA, Smit MA, i dr. Metodologicheskij podhod k razrabotke dozimetricheskih modelej skeleta cheloveka dlya beta-izluchayushhih radionuklidov. Radiacionnaya gigiena. 2019; 12 (2). DOI: 10.21514/1998-426X-2019-12-2-66-75. Russian.
15. Volchkova AYu, Sharagin PA, Shishkina EA. Internal bone marrow dosimetry: the effect of the exposure due to 90Sr incorporated in the adjacent bone segments. Bulletin of the South Ural State University. Ser. Mathematical Modelling, Programming & Computer Software. 2022; 15 (4): 44–58. DOI: 10.14529/mmp220404.
16. Sharagin PA, Shishkina EA, Tolstykh EI. Vychislitel'nyj fantom dlya dozimetrii krasnogo kostnogo mozga novorozhdennogo rebenka ot inkorporirovannyh beta-izluchatelej. Medicina ehkstremal'nyh situacij. 2022; (4): 74–82. DOI: 10.47183/mes.2022.045. Russian.
17. Cristy M. Active bone marrow distribution as a function of age in humans. Phys Med Biol. 1981; 26 (3): 389–400.
18. Sharagin PA, Shishkina EA, Tolstykh EI, Volchkova AYu, Smith MA, Degteva MO. Segmentation of hematopoietic sites of human skeleton for calculations of dose to active marrow exposed to bone-seeking radionuclides. RAD Conference Proceedings. 2018; (3): 154–8. DOI: 10.21175/RadProc.2018.33.
19. Sharagin PA, Tolstykh EI, Shishkina EA, Degteva MO. Dozimetricheskoe modelirovanie kosti dlya osteotropnyh beta-izluchayushhih radionuklidov: razmernye parametry i segmentaciya. V sbornike: Materialy mezhdunarodnoj nauchnoj konferencii “Sovremennye problemy radiobiologii”. Belarus', Gomel', 23-24 sentyabrya 2021; s. 200–204. Russian.
20. Tolstykh EI, Sharagin PA, Shishkina EA, Degteva MO. Formirovanie doz oblucheniya krasnogo kostnogo mozga cheloveka ot 89,90Sr, ocenka parametrov trabekulyarnoj kosti dlya dozimetricheskogo modelirovaniya. V sbornike: Materialy mezhdunarodnoj nauchnoj konferencii “Sovremennye problemy radiobiologii”. Belarus', Gomel', 23–24 sentyabrya 2021; s. 176–179. Russian.
21. Tolstykh EI, Sharagin PA, Shishkina EA, Volchkova AYu, Degteva MO. Anatomo-morfologicheskij bazis dlya dozimetricheskogo modelirovaniya trabekulyarnoj kosti cheloveka s ispol'zovaniem stoxasticheskogo parametricheskogo podhoda. Klinicheskij vestnik GNC FMBC im. A. I. Burnazyana. 2022; 3: 25–40. Russian.
22. Valentin J. Basic anatomical and physiological data for use in radiological protection: reference values. Annals of the ICRP. Annals of the ICRP. 2002; 32 (3–4): 1–277.
23. Shishkina EA, Timofeev YS, Volchkova AY, Sharagin PA, Zalyapin VI, Degteva MO, et al. Trabecula: a random generator of computational phantoms for bone marrow dosimetry. Health Phys. 2020; 118 (1): 53–59. DOI: 10.1097/HP.0000000000001127.
24. Zalyapin VI, Timofeev YuS, Shishkina EA. A parametric stochastic model of bone geometry. Bulletin of Southern Urals State University, Issue «Mathematical Modelling. Programming & Computer Software» (SUSU MMCS) 2018; 11 (2): 44–57. DOI: 10.14529/mmp180204.
25. Robinson RA. Chemical analysis and electron microscopy of bone. In: Rodahl K, Nicholson JT, Brown EM editors. Bone as a tissue. New York: McGraw-Hill, 1960; p. 186–250.
26. Vogler JB 3rd, Murphy WA. Bone marrow imaging. Radiology. 1988; 168 (3): 679–93.
27. Vande Berg BC, Malghem J, Lecouvet FE, Maldague B. Magnetic resonance imaging of the normal bone marrow. Skeletal Radiology. 1998; 27: 471–83.
28. Vande Berg BC, Malghem J, Lecouvet FE, Maldague B. Magnetic resonance imaging of normal bone marrow. Eur Radiol. 1998; 8 (8): 1327–34.
29. Taccone A, Oddone M, Dell'Acqua AD, Occhi M, Ciccone MA. MRI "road–map" of normal age-related bone marrow. II. Thorax, pelvis and extremities. Pediatr Radiol. 1995; 25 (8): 596–606; PubMed PMID: 8570312.
30. Taccone A, Oddone M, Occhi M, Dell'Acqua AD, Ciccone MA. MRI "road–map" of normal age-related bone marrow. I. Cranial bone and spine. Pediatr Radiol. 1995; 25 (8): 588–95; PubMed PMID: 8570311.
31. Cunningham C, Scheuer L, Black S. Developmental juvenile osteology. Elsevier Academic Press, 2016.
32. Ryan TM, Krovitz GE. Trabecular bone ontogeny in the human proximal femur. J Hum Evol. 2006; 51 (6): 591–602.
33. Milovanovic P, Djonic D, Hahn M, Amling M, Busse B, Djuric M. Region-dependent patterns of trabecular bone growth in the human proximal femur: A study of 3D bone microarchitecture from early postnatal to late childhood period. Am J Phys Anthropol. 2017; 164 (2): 281–91. DOI: 10.1002/ajpa.23268. Epub 2017 Jun 20.
34. Saers JP, Cazorla-Bak Y, Shaw CN, Stock JT, Ryan TM. Trabecular bone structural variation throughout the human lower limb. J Hum Evol. 2016; 97: 97–108. DOI: 10.1016/j.jhevol.2016.05.012.
35. Ryan TM, Raichlen DA, Gosman JH. Structural and mechanical changes in trabecular bone during early development in the human femur and humerus. In: Building bones: bone formation and development in anthropology. Cambridge University Press, 2017; p. 281–302. Available from: https://doi.org/10.1017/9781316388907.013.
36. Byers S, Moore AJ, Byard RW, Fazzalari NL. Quantitative histomorphometric analysis of the human growth plate from birth to adolescence. Bone. 2000; 27 (4): 495–501.
37. Gosman JH, Ketcham RA. Patterns in ontogeny of human trabecular bone from SunWatch Village in the Prehistoric Ohio Valley: general features of microarchitectural change. Am J Phys Anthropol. 2009; 138 (3): 318–32. DOI: 10.1002/ajpa.20931. PubMed PMID: 18785633.
38. Volpato V. Bone endostructure morphogenesis of the human ilium. Comptes rendus Palévol. 2008; 7: 463–71. DOI: 10.1016/j.crpv.2008.06.001.
39. Glorieux FH, Travers R, Taylor A, Bowen JR, Rauch F, Norman M, et al. Normative data for iliac bone histomorphometry in growing children. Bone. 2000; 26 (2): 103–9.
40. Rodriguez-Florez N, Ibrahim A, Hutchinson JC, Borghi A, James G, Arthurs OJ, et al. Cranial bone structure in children with sagittal craniosynostosis: relationship with surgical outcomes. J Plast Reconstr Aesthet Surg. 2017; 70 (11): 1589–97. DOI: 10.1016/j.bjps.2017.06.017.
41. Hough M, Johnson P, Rajon D, Jokisch D, Lee C, Bolch W. An image-based skeletal dosimetry model for the ICRP reference adult male—internal electron sources. Phys Med Biol. 2011; 56 (8): 2309–46.
42. Acquaah F, Robson Brown KA, Ahmed F, Jeffery N, Abel RL. Early trabecular development in human vertebrae: overproduction, constructive regression, and refinement. Front Endocrinol (Lausanne). 2015; 6: 67. DOI: 10.3389/fendo.2015.00067. eCollection 2015.
43. Florence JL. Linear and cortical bone dimensions as indicators of health status in subadults from the Milwaukee County Poor Farm Cemetery. M.A., University of Colorado at Denver, 2007.
44. Miles AEW. Growth cuves of immature bones from a scottish island population of sixteenth to mid-nineteenth century: limb-bone diaphyses and some bones of the hand and foot. International Journal of Osteoarcheology. 1994; 4: 121–36.
45. Maresh MM. Measurements from roentgenograms. In: McCammon RW, editor. Human Growth and Development. Springfield, IL: Charles C. Thomas, 1970; p. 157–200.
46. Dhavale N, Halcrow SE, Buckley HR, Tayles N, Domett KM, Gray AR. Linear and appositional growth in infants and children from the prehistoric settlement of Ban Non Wat, Northeast Thailand: evaluating biological responses to agricultural intensification in Southeast Asia. Journal of Archaeological Science: Reports. 2017; 11: 435–46.
47. Svadovsky VS. Age-related bone remodeling. Moscow, 1961.
48. Danforth ME, Wrobel GD, Armstrong CW, Swanson D. Juvenile age estimation using diaphyseal long bone lengths among ancient Maya populations. Latin American Antiquity. 2017; 20 (1): 3–13.
49. Beresheim AC, Pfeiffer S, Grynpas M. Ontogenetic changes to bone microstructure in an archaeologically derived sample of human ribs. J Anat. 2019. DOI: 10.1111/joa.13116
50. Pfeiffer S. Cortical Bone Histology in Juveniles. Available from: https://www.researchgate.net/publication/303179375_Cortical_bone_histology_in_Juveniles
51. Hresko AM, Hinchcliff EM, Deckey DG, Hresko MT. Developmental

sacral morphology: MR study from infancy to skeletal maturity. Eur Spine J. 2020. Available from: https://doi.org/10.1007/s00586-020-06350-6.
52. Kuznecov LE. Perelomy taza u detej: morfologiya, biomexanika, diagnostika. M.: Folium, 1994. Russian.
53. Mavrych V, Bolgova O, Ganguly P, Kashchenko S. Age-related changes of lumbar vertebral body morphometry. Austin J Anat. 2014; 1 (3): 7.
54. Dimeglio A, Bonnel F, Canavese F. The Growing Spine. In: Jean Marc Vital, Derek Thomas Cawley, editors. Spinal Anatomy. Modern Concepts. Springer, 2020; p. 25–52.
55. Andronevsky A. Anatomy rebenka. Buharest: Meridian, 1970.
56. Bernert Zs, Évinger S, Hajdu T. New data on the biological age estimation of children using bone measurements based on historical populations from the Carpathian Basin. Annales Historico-Naturales Musei Nationalis Hungarici. 2007; 99: 199–206.
57. Gindhart PS. Growth standards for the tibia and radius in children aged one month through eighteen years. Am J Phys Anthrop. 1973; 39: 41–48.
58. Lopez-Costas O, Rissech C, Trancho G, Turbón D. Postnatal ontogenesis of the tibia. Implications for age and sex estimation. Forensic Sci Int. 2012; 214 (1–3): 207.e1–11. DOI: 10.1016/j.forsciint.2011.07.038. Epub 2011 Aug 20. PubMed PMID: 21862250.
59. Blake KAS. An investigation of sex determination from the subadult pelvis: a morphometric analysis. Doctoral Dissertation, University of Pittsburgh. 2011.
60. Cunningham CA, Black SM. Iliac cortical thickness in the neonate - the gradient effect. J Anat. 2009; 215 (3): 364–70. DOI: 10.1111/j.1469-7580.2009.01112.x.
61. Cunningham CA, Black SM. Anticipating bipedalism: trabecular organization in the newborn ilium. J Anat. 2009; 214 (6): 817–29. DOI: 10.1111/j.1469-7580.2009.01073.x
62. Corron L, Marchal F, Condemi S, Chaumoître K, Adalian P. A New Approach of Juvenile Age Estimation using Measurements of the Ilium and Multivariate Adaptive Regression Splines (MARS) Models for Better Age Prediction. Forensic Sci. 2017; 62 (1): 18–29. DOI: 10.1111/1556-4029.13224.
63. Parfitt AM, Travers R, Rauch F, Glorieux FH. Structural and cellular changes during bone growth in healthy children. Bone. 2000; 27 (4): 487–94. PMID: 11033443.
64. Schnitzler CM, Mesquita JM, Pettifor JM. Cortical bone development in black and white South African children: iliac crest histomorphometry. Bone. 2009; 44 (4): 603–11. DOI: 10.1016/j.bone.2008.12.009.
65. De Boer HH, Van der Merwe AE, Soerdjbalie-Maikoe VV. Human cranial vault thickness in a contemporary sample of 1097 autopsy cases: relation to body weight, stature, age, sex and ancestry. Int J Legal Med. 2016; 130 (5): 1371–7. DOI: 10.1007/s00414-016-1324-5.
66. Margulies S, Coats B. Experimental injury biomechanics of the pediatric head and brain. Chapter 4. In: Crandall JR, Myers BS, Meaney DF, Schmidtke SZ, editors. Pediatric Injury Biomechanics Springer Science + Business Media New York. 2013; p. 157–190.
67. Li Z, Park BK, Liu W, Zhang J, Reed MP, Rupp JD, et al. A statistical skull geometry model for children 0–3 years old. PLoS One. 2015 May 18; 10 (5): e0127322. DOI: 10.1371/journal.pone.0127322. eCollection 2015.
68. Rodriguez-Florez N, Ibrahim A, Hutchinson JC, Borghi A, James G, Arthurs OJ, et al. Cranial bone structure in children with sagittal craniosynostosis: Relationship with surgical outcomes. J Plast Reconstr Aesthet Surg. 2017; 70 (11): 1589–97. DOI: 10.1016/j.bjps.2017.06.017.
69. McGraw MA, Mehlman CT, Lindsell CJ, Kirby CL. Postnatal growth of the clavicle: birth to eighteen years of age. Journal of Pediatric Orthopedics. 2009; 29: 937.
70. Bleuze MM, Wheeler SM, Williams LJ, Dupras TL. Growth of the pectoral girdle in a sample of juveniles from the kellis 2 cemetery, Dakhleh Oasis, Egypt. Am J Hum Biol. 2016; 28 (5): 636–45.
71. Black SM, Scheuer JL. Age changes in the clavicle: from the early neonatal period to skeletal maturity. International Journal of Osteoarchaeology. 1996; 6: 425–34.
72. Bernat A, Huysmans T, Van Glabbeek F, Sijbers J, Gielen J, Van Tongel A. The anatomy of the clavicle: a three-dimensional cadaveric study. Clin Anat. 2014; 27 (5): 712–23.
73. Vallois HV. L'omoplate humaine. Bulletin de la Sociétié d'Anthropolgie de Paris. 1946; 7: 16–99.
74. Saunders S, Hoppa R, Southern R. Diaphyseal growth in a nineteenth-century skeletal sample of subadults from St Thomas' Church, Belleville, Ontario. International Journal of Osteoarchaeology. 1993; 3: 265–81.
75. Rissech C, Black S. Scapular development from neonatal period to skeletal maturity. A preliminary study. Int J Osteoarchaeol. 2007; 17: 451–64.
76. Cardoso HFV, Spake L, Humphrey LT. Age estimation of immature human skeletal remains from the dimensions of the girdle bones in the postnatal period. Am J Phys Anthropol. 2017; 163 (4): 772–83. DOI: 10.1002/ajpa.23248. Epub 2017 May 24. PubMed PMID: 28542741.
77. Badr El Dine F, Hassan H. Ontogenetic study of the scapula among some Egyptians: Forensic implications in age and sex estimation using Multidetector Computed Tomography, Egyptian Journal of Forensic Sciences. 2015; 6 (2): 56–77.
78. Kneissel M, Roschger P, Steiner W, Schamall D, Kalchhauser G, Boyde A, et al. Cancellous Bone Structure in the Growing and Aging Lumbar Spine in a Historic Nubian Population. Calcif Tissue Int. 1997; 61: 95–100.
79. Johnson KT, Al-Holou WN, Anderson RC, Wilson TJ, Karnati T, Ibrahim M, et al. Morphometric analysis of the developing pediatric cervical spine. J Neurosurg Pediatr. 2016; 18 (3): 377–89. DOI: 10.3171/2016.3. PEDS1612. Epub 2016 May 27. PubMed PMID: 27231821.
80. Comeau A. Age-related changes in geometric characteristics of the pediatric thoracic cage and comparison of thorax shape with a pediatric CPR Manikin. PhD thesis. 2010.

Литература

1. Degteva MO, Shagina NB, Vorobiova MI, Shishkina EA, Tolstykh EI, Akleyev AV. Contemporary Understanding of Radioactive Contamination of the Techa River in 1949-1956. Radiats Biol Radioecol. 2016; 56 (5): 523–34.PMID: 30703313. Russian.
2. Krestinina LY, Epifanova S, Silkin S, Mikryukova L, Degteva M, Shagina N, et al. Chronic low-dose exposure in the Techa River Cohort: risk of mortality from circulatory diseases. Radiat Environ Biophys. 2013; 52 (1): 47–57. DOI: 10.1007/s00411-012-0438-5. Epub 2012 Nov 4.
3. Аклеев А. В. Хронический лучевой синдром у жителей прибрежных сел реки Теча. Челябинск: Книга, 2012; 464 с.
4. Preston DL, Sokolnikov ME, Krestinina LY, Stram DO. Estimates of radiation effects on cancer risks in the mayak worker, Techa river and atomic bomb survivor studies. Radiat Prot Dosimetry. 2017; 173 (1–3): 26–31. DOI: 10.1093/rpd/ncw316.
5. Degteva MO, Napier BA, Tolstykh EI, et al. Enhancements in the Techa river dosimetry system: TRDS-2016D Code for reconstruction of deterministic estimates of dose from environmental exposures. Health Phys. 2019; 117 (4): 378–87. DOI: 10.1097/HP.0000000000001067.
6. Spiers FW, Beddoe AH, Whitwell JR. Mean skeletal dose factors for beta-particle emitters in human bone. Part I: volume-seeking radionuclides. The British journal of radiology. 1978; 51 (608): 622–7.
7. Силкин С. С., Крестинина Л. Ю., Старцев Н. В, Аклеев А. В. Уральская когорта аварийно-облученного населения. Медицина экстремальных ситуаций. 2019; 21 (3): 393–402.
8. O'Reilly SE, DeWeese LS, Maynard MR, Rajon DA, Wayson MB, Marshall EL, et al. An 13 image-based skeletal dosimetry model for the ICRP reference adult female-internal electron 14 sources. Phys Med Biol. 2016 Dec 21; 61 (24): 8794–824. Epub 2016 Nov 29.
9. Xu XG, Chao TC, Bozkurt A. VIP-Man: an image-based whole-body adult male model constructed from color photographs of the Visible Human Project for multi-particle Monte Carlo calculations.

Health Phys. 2000; 78 (5): 476–86. DOI: 10.1097/00004032-200005000-00003. PMID: 10772019.
10. Shah AP, Bolch WE, Rajon DA, Patton PW, Jokisch DW. A paired-image radiation transport model for skeletal dosimetry. J Nucl Med. 2005; 46 (2): 344–53. PMID: 15695796.
11. Pafundi D. Image-based skeletal tissues and electron dosimetry models for the ICRP reference pediatric age series. A dissertation presented to the graduate schools of the University of Florida in partial fulfillment of the requirements for the degree of doctor of the philosophy. University of Florida. 2009.
12. Hough M, Johnson P, Rajon D, Jokisch D, Lee C, Bolch W. An image-based skeletal dosimetry model for the ICRP reference adult male–internal electron sources. Phys Med Biol. 2011; 56 (8): 2309–46. DOI: 10.1088/0031-9155/56/8/001.
13. Degteva MO, Tolstykh EI, Shishkina EA, Sharagin PA, Zalyapin VI, Volchkova AYu, et al. PLoS One. 2021; 16 (10): e0257605. DOI: 10.1371/journal.pone.0257605. PMID: 34648511; PMCID: PMC8516275.PlosOne.
14. Дёгтева М. О., Шишкина Е. А., Толстых Е. И., Заляпин В. И., Шарагин П. А., Смит М. А., и др. Методологический подход к разработке дозиметрических моделей скелета человека для бета-излучающих радионуклидов. Радиационная гигиена. 2019; 12 (2). DOI: 10.21514/1998-426X-2019-12-2-66-75.
15. Volchkova AYu, Sharagin PA, Shishkina EA. Internal bone marrow dosimetry: the effect of the exposure due to 90Sr incorporated in the adjacent bone segments. Bulletin of the South Ural State University. Ser. Mathematical Modelling, Programming & Computer Software. 2022; 15 (4): 44–58. DOI: 10.14529/mmp220404.
16. Шарагин П. А., Шишкина Е. А., Толстых Е. И. Вычислительный фантом для дозиметрии красного костного мозга новорожденного ребенка от инкорпорированных бета-излучателей. Медицина экстремальных ситуаций. 2022; (4): 74–82. DOI: 10.47183/mes.2022.045.
17. Cristy M. Active bone marrow distribution as a function of age in humans. Phys Med Biol. 1981; 26 (3): 389–400.
18. Sharagin PA, Shishkina EA, Tolstykh EI, Volchkova AYu, Smith MA, Degteva MO. Segmentation of hematopoietic sites of human skeleton for calculations of dose to active marrow exposed to bone-seeking radionuclides. RAD Conference Proceedings. 2018; (3): 154–8. DOI: 10.21175/RadProc.2018.33.
19. Шарагин П. А., Толстых Е. И., Шишкина Е. А., Дегтева М. О. Дозиметрическое моделирование кости для остеотропных бета-излучающих радионуклидов: размерные параметры и сегментация. В сборнике: Материалы международной научной конференции “Современные проблемы радиобиологии”. Беларусь, Гомель, 23-24 сентября 2021; с. 200–204.
20. Толстых Е. И., Шарагин П. А., Шишкина Е. А., Дегтева М. О. Формирование доз облучения красного костного мозга человека от 89,90Sr, оценка параметров трабекулярной кости для дозиметрического моделирования. В сборнике: Материалы международной научной конференции “Современные проблемы радиобиологии”. Беларусь, Гомель, 23–24 сентября 2021; с. 176–179.
21. Толстых Е. И., Шарагин П. А., Шишкина Е. А., Волчкова А. Ю. Дегтева М. О. Анатомо-морфологический базис для дозиметрического моделирования трабекулярной кости человека с использованием стохастического параметрического подхода. Клинический вестник ГНЦ ФМБЦ им. А. И. Бурназяна. 2022; 3: 25–40.
22. Valentin J. Basic anatomical and physiological data for use in radiological protection: reference values. Annals of the ICRP. Annals of the ICRP. 2002; 32 (3–4): 1–277.
23. Shishkina EA, Timofeev YS, Volchkova AY, Sharagin PA, Zalyapin VI, Degteva MO, et al. Trabecula: a random generator of computational phantoms for bone marrow dosimetry. Health Phys. 2020; 118 (1): 53–59. DOI: 10.1097/HP.0000000000001127.
24. Zalyapin VI, Timofeev YuS, Shishkina EA. A parametric stochastic model of bone geometry. Bulletin of Southern Urals State University, Issue «Mathematical Modelling. Programming & Computer Software» (SUSU MMCS) 2018; 11 (2): 44–57. DOI: 10.14529/mmp180204.
25. Robinson RA. Chemical analysis and electron microscopy of bone. In: Rodahl K, Nicholson JT, Brown EM editors. Bone as a tissue. New York: McGraw-Hill, 1960; p. 186–250.
26. Vogler JB 3rd, Murphy WA. Bone marrow imaging. Radiology. 1988; 168 (3): 679–93.
27. Vande Berg BC, Malghem J, Lecouvet FE, Maldague B. Magnetic resonance imaging of the normal bone marrow. Skeletal Radiology. 1998; 27: 471–83.
28. Vande Berg BC, Malghem J, Lecouvet FE, Maldague B. Magnetic resonance imaging of normal bone marrow. Eur Radiol. 1998; 8 (8): 1327–34.
29. Taccone A, Oddone M, Dell'Acqua AD, Occhi M, Ciccone MA. MRI "road–map" of normal age-related bone marrow. II. Thorax, pelvis and extremities. Pediatr Radiol. 1995; 25 (8): 596–606; PubMed PMID: 8570312.
30. Taccone A, Oddone M, Occhi M, Dell'Acqua AD, Ciccone MA. MRI "road–map" of normal age-related bone marrow. I. Cranial bone and spine. Pediatr Radiol. 1995; 25 (8): 588–95; PubMed PMID: 8570311.
31. Cunningham C, Scheuer L, Black S. Developmental juvenile osteology. Elsevier Academic Press, 2016.
32. Ryan TM, Krovitz GE. Trabecular bone ontogeny in the human proximal femur. J Hum Evol. 2006; 51 (6): 591–602.
33. Milovanovic P, Djonic D, Hahn M, Amling M, Busse B, Djuric M. Region-dependent patterns of trabecular bone growth in the human proximal femur: A study of 3D bone microarchitecture from early postnatal to late childhood period. Am J Phys Anthropol. 2017; 164 (2): 281–91. DOI: 10.1002/ajpa.23268. Epub 2017 Jun 20.
34. Saers JP, Cazorla-Bak Y, Shaw CN, Stock JT, Ryan TM. Trabecular bone structural variation throughout the human lower limb. J Hum Evol. 2016; 97: 97–108. DOI: 10.1016/j.jhevol.2016.05.012.
35. Ryan TM, Raichlen DA, Gosman JH. Structural and mechanical changes in trabecular bone during early development in the human femur and humerus. In: Building bones: bone formation and development in anthropology. Cambridge University Press, 2017; p. 281–302. Available from: https://doi.org/10.1017/9781316388907.013.
36. Byers S, Moore AJ, Byard RW, Fazzalari NL. Quantitative histomorphometric analysis of the human growth plate from birth to adolescence. Bone. 2000; 27 (4): 495–501.
37. Gosman JH, Ketcham RA. Patterns in ontogeny of human trabecular bone from SunWatch Village in the Prehistoric Ohio Valley: general features of microarchitectural change. Am J Phys Anthropol. 2009; 138 (3): 318–32. DOI: 10.1002/ajpa.20931. PubMed PMID: 18785633.
38. Volpato V. Bone endostructure morphogenesis of the human ilium. Comptes rendus Palévol. 2008; 7: 463–71. DOI: 10.1016/j.crpv.2008.06.001.
39. Glorieux FH, Travers R, Taylor A, Bowen JR, Rauch F, Norman M, et al. Normative data for iliac bone histomorphometry in growing children. Bone. 2000; 26 (2): 103–9.
40. Rodriguez-Florez N, Ibrahim A, Hutchinson JC, Borghi A, James G, Arthurs OJ, et al. Cranial bone structure in children with sagittal craniosynostosis: relationship with surgical outcomes. J Plast Reconstr Aesthet Surg. 2017; 70 (11): 1589–97. DOI: 10.1016/j.bjps.2017.06.017.
41. Hough M, Johnson P, Rajon D, Jokisch D, Lee C, Bolch W. An image-based skeletal dosimetry model for the ICRP reference adult male—internal electron sources. Phys Med Biol. 2011; 56 (8): 2309–46.
42. Acquaah F, Robson Brown KA, Ahmed F, Jeffery N, Abel RL. Early trabecular development in human vertebrae: overproduction, constructive regression, and refinement. Front Endocrinol (Lausanne). 2015; 6: 67. DOI: 10.3389/fendo.2015.00067. eCollection 2015.
43. Florence JL. Linear and cortical bone dimensions as indicators of health status in subadults from the Milwaukee County Poor Farm Cemetery. M.A., University of Colorado at Denver, 2007.
44. Miles AEW. Growth cuves of immature bones from a scottish island population of sixteenth to mid-nineteenth century: limb-bone diaphyses and some bones of the hand and foot. International Journal of Osteoarcheology. 1994; 4: 121–36.
45. Maresh MM. Measurements from roentgenograms. In: McCammon RW, editor. Human Growth and Development.

Springfield, IL: Charles C. Thomas, 1970; p. 157–200.
46. Dhavale N, Halcrow SE, Buckley HR, Tayles N, Domett KM, Gray AR. Linear and appositional growth in infants and children from the prehistoric settlement of Ban Non Wat, Northeast Thailand: evaluating biological responses to agricultural intensification in Southeast Asia. Journal of Archaeological Science: Reports. 2017; 11: 435–46.
47. Svadovsky VS. Age-related bone remodeling. Moscow, 1961.
48. Danforth ME, Wrobel GD, Armstrong CW, Swanson D. Juvenile age estimation using diaphyseal long bone lengths among ancient Maya populations. Latin American Antiquity. 2017; 20 (1): 3–13.
49. Beresheim AC, Pfeiffer S, Grynpas M. Ontogenetic changes to bone microstructure in an archaeologically derived sample of human ribs. J Anat. 2019. DOI: 10.1111/joa.13116
50. Pfeiffer S. Cortical Bone Histology in Juveniles. Available from: https://www.researchgate.net/publication/303179375_Cortical_bone_histology_in_Juveniles
51. Hresko AM, Hinchcliff EM, Deckey DG, Hresko MT. Developmental sacral morphology: MR study from infancy to skeletal maturity. Eur Spine J. 2020. Available from: https://doi.org/10.1007/s00586-020-06350-6.
52. Кузнецов Л. Е. Переломы таза у детей: морфология, биомеханика, диагностика. М.: Фолиум, 1994.
53. Mavrych V, Bolgova O, Ganguly P, Kashchenko S. Age-related changes of lumbar vertebral body morphometry. Austin J Anat. 2014; 1 (3): 7.
54. Dimeglio A, Bonnel F, Canavese F. The Growing Spine. In: Jean Marc Vital, Derek Thomas Cawley, editors. Spinal Anatomy. Modern Concepts. Springer, 2020; p. 25–52.
55. Андроневский А. Анатомия ребенка. Бухарест: Меридиан, 1970.
56. Bernert Zs, Évinger S, Hajdu T. New data on the biological age estimation of children using bone measurements based on historical populations from the Carpathian Basin. Annales Historico-Naturales Musei Nationalis Hungarici. 2007; 99: 199–206.
57. Gindhart PS. Growth standards for the tibia and radius in children aged one month through eighteen years. Am J Phys Anthrop. 1973; 39: 41–48.
58. Lopez-Costas O, Rissech C, Trancho G, Turbón D. Postnatal ontogenesis of the tibia. Implications for age and sex estimation. Forensic Sci Int. 2012; 214 (1–3): 207.e1–11. DOI: 10.1016/j.forsciint.2011.07.038. Epub 2011 Aug 20. PubMed PMID: 21862250.
59. Blake KAS. An investigation of sex determination from the subadult pelvis: a morphometric analysis. Doctoral Dissertation, University of Pittsburgh. 2011.
60. Cunningham CA, Black SM. Iliac cortical thickness in the neonate - the gradient effect. J Anat. 2009; 215 (3): 364–70. DOI: 10.1111/j.1469-7580.2009.01112.x.
61. Cunningham CA, Black SM. Anticipating bipedalism: trabecular organization in the newborn ilium. J Anat. 2009; 214 (6): 817–29. DOI: 10.1111/j.1469-7580.2009.01073.x
62. Corron L, Marchal F, Condemi S, Chaumoître K, Adalian P. A New Approach of Juvenile Age Estimation using Measurements of the Ilium and Multivariate Adaptive Regression Splines (MARS) Models for Better Age Prediction. Forensic Sci. 2017; 62 (1): 18–29. DOI: 10.1111/1556-4029.13224.
63. Parfitt AM, Travers R, Rauch F, Glorieux FH. Structural and cellular changes during bone growth in healthy children. Bone. 2000; 27 (4): 487–94. PMID: 11033443.
64. Schnitzler CM, Mesquita JM, Pettifor JM. Cortical bone development in black and white South African children: iliac crest histomorphometry. Bone. 2009; 44 (4): 603–11. DOI: 10.1016/j.bone.2008.12.009.
65. De Boer HH, Van der Merwe AE, Soerdjbalie-Maikoe VV. Human cranial vault thickness in a contemporary sample of 1097 autopsy cases: relation to body weight, stature, age, sex and ancestry. Int J Legal Med. 2016; 130 (5): 1371–7. DOI: 10.1007/s00414-016-1324-5.
66. Margulies S, Coats B. Experimental injury biomechanics of the pediatric head and brain. Chapter 4. In: Crandall JR, Myers BS, Meaney DF, Schmidtke SZ, editors. Pediatric Injury Biomechanics Springer Science + Business Media New York. 2013; p. 157–190.
67. Li Z, Park BK, Liu W, Zhang J, Reed MP, Rupp JD, et al. A statistical skull geometry model for children 0–3 years old. PLoS One. 2015 May 18; 10 (5): e0127322. DOI: 10.1371/journal.pone.0127322. eCollection 2015.
68. Rodriguez-Florez N, Ibrahim A, Hutchinson JC, Borghi A, James G, Arthurs OJ, et al. Cranial bone structure in children with sagittal craniosynostosis: Relationship with surgical outcomes. J Plast Reconstr Aesthet Surg. 2017; 70 (11): 1589–97. DOI: 10.1016/j.bjps.2017.06.017.
69. McGraw MA, Mehlman CT, Lindsell CJ, Kirby CL. Postnatal growth of the clavicle: birth to eighteen years of age. Journal of Pediatric Orthopedics. 2009; 29: 937.
70. Bleuze MM, Wheeler SM, Williams LJ, Dupras TL. Growth of the pectoral girdle in a sample of juveniles from the kellis 2 cemetery, Dakhleh Oasis, Egypt. Am J Hum Biol. 2016; 28 (5): 636–45.
71. Black SM, Scheuer JL. Age changes in the clavicle: from the early neonatal period to skeletal maturity. International Journal of Osteoarchaeology. 1996; 6: 425–34.
72. Bernat A, Huysmans T, Van Glabbeek F, Sijbers J, Gielen J, Van Tongel A. The anatomy of the clavicle: a three-dimensional cadaveric study. Clin Anat. 2014; 27 (5): 712–23.
73. Vallois HV. L'omoplate humaine. Bulletin de la Sociétié d'Anthropolgie de Paris. 1946; 7: 16–99.
74. Saunders S, Hoppa R, Southern R. Diaphyseal growth in a nineteenth-century skeletal sample of subadults from St Thomas' Church, Belleville, Ontario. International Journal of Osteoarchaeology. 1993; 3: 265–81.
75. Rissech C, Black S. Scapular development from neonatal period to skeletal maturity. A preliminary study. Int J Osteoarchaeol. 2007; 17: 451–64.
76. Cardoso HFV, Spake L, Humphrey LT. Age estimation of immature human skeletal remains from the dimensions of the girdle bones in the postnatal period. Am J Phys Anthropol. 2017; 163 (4): 772–83. DOI: 10.1002/ajpa.23248. Epub 2017 May 24. PubMed PMID: 28542741.
77. Badr El Dine F, Hassan H. Ontogenetic study of the scapula among some Egyptians: Forensic implications in age and sex estimation using Multidetector Computed Tomography, Egyptian Journal of Forensic Sciences. 2015; 6 (2): 56–77.
78. Kneissel M, Roschger P, Steiner W, Schamall D, Kalchhauser G, Boyde A, et al. Cancellous Bone Structure in the Growing and Aging Lumbar Spine in a Historic Nubian Population. Calcif Tissue Int. 1997; 61: 95–100.
79. Johnson KT, Al-Holou WN, Anderson RC, Wilson TJ, Karnati T, Ibrahim M, et al. Morphometric analysis of the developing pediatric cervical spine. J Neurosurg Pediatr. 2016; 18 (3): 377–89. DOI: 10.3171/2016.3. PEDS1612. Epub 2016 May 27. PubMed PMID: 27231821.
80. Comeau A. Age-related changes in geometric characteristics of the pediatric thoracic cage and comparison of thorax shape with a pediatric CPR Manikin. PhD thesis. 2010.